

BICEP/Keck XXI: Constraints on Early-Universe Parity Violation from Multipole-Dependent Birefringence

P. A. R. Ade,¹ Z. Ahmed ^{2,3} M. Amiri ⁴ D. Barkats ⁵ R. Basu Thakur ⁶ C. A. Bischoff ⁷ D. Beck ^{8,*} J. J. Bock,^{6,9} H. Boenish,⁵ V. Buza,¹⁰ B. Cantrall ^{8,2} J. R. Cheshire IV ⁶ J. Connors,¹¹ J. Cornelison ¹² M. Crumrine,¹³ A. J. Cukierman,⁶ E. Denison,¹¹ L. Duband,¹⁴ M. Echter,⁵ M. Eiben ¹⁵ B. D. Elwood ^{5,16} S. Fatigoni ⁶ J. P. Filippini ¹⁷ A. Fortes,⁸ M. Gao,⁶ C. Giannakopoulos,⁷ N. Goeckner-Wald,⁸ D. C. Goldfinger ⁸ S. Gratton,^{18,19} J. A. Grayson,⁸ A. Greathouse ⁶ P. K. Grimes ⁵ G. Hall,^{20,8} G. Halal ⁸ M. Halpern,⁴ E. Hand,⁷ S. A. Harrison,⁵ S. Henderson,^{2,3} T. D. Hoang ¹³ J. Hubmayr,¹¹ H. Hui ⁶ K. D. Irwin,⁸ J. H. Kang ⁶ K. S. Karkare ²¹ S. Kefeli,⁶ J. M. Kovac ^{5,16} C. Kuo,⁸ K. Lasko ^{13,20} K. Lau ⁶ M. Lautzenhiser,⁷ A. Lennox,¹⁷ T. Liu ^{8,†} S. C. Mackey ^{10,22} N. Maher,¹³ K. G. Megerian,⁹ L. Minutolo,⁶ L. Moncelsi ⁶ Y. Nakato,⁸ H. T. Nguyen,^{6,9} R. O'Brient,^{6,9} S. N. Paine,⁵ A. Patel,⁶ M. A. Petroff ⁵ A. R. Polish ^{5,16} T. Prouve,¹⁴ C. Pryke ¹³ C. D. Reintsema,¹¹ S. Richter,⁵ T. Romand,⁶ M. Salatino,⁸ A. Schillaci,⁶ B. Schmitt,⁵ R. Schwartz,¹³ C. D. Sheehy,¹³ B. Singari ^{13,20} A. Soliman,^{6,9} T. St. Germaine,⁵ A. Steiger ⁶ B. Steinbach,⁶ R. Sudiwala,¹ G. Teply,⁶ K. L. Thompson,^{2,8} C. Tucker ¹ A. D. Turner,⁹ C. Vergès ²³ A. G. Viereg, ^{10,22} A. Wandui ⁶ A. C. Weber,⁹ J. Willmert ¹³ C. L. Wong,^{5,16} W. L. K. Wu ^{2,3} H. Yang,⁸ C. Yu ^{10,12} L. Zheng ⁵ C. Zhang ² and S. Zhang⁶

¹*School of Physics and Astronomy, Cardiff University, Cardiff, CF24 3AA, United Kingdom*

²*Kavli Institute for Particle Astrophysics and Cosmology, Stanford University, Stanford, CA 94305, USA*

³*SLAC National Accelerator Laboratory, Menlo Park, CA 94025, USA*

⁴*Department of Physics and Astronomy, University of British Columbia, Vancouver, British Columbia, V6T 1Z1, Canada*

⁵*Center for Astrophysics, Harvard & Smithsonian, Cambridge, MA 01238, USA*

⁶*Department of Physics, California Institute of Technology, Pasadena, CA 91125, USA*

⁷*Department of Physics, University of Cincinnati, Cincinnati, OH 45221, USA*

⁸*Department of Physics, Stanford University, Stanford, CA 94305, USA*

⁹*Jet Propulsion Laboratory, California Institute of Technology, Pasadena, CA 91109, USA*

¹⁰*Kavli Institute for Cosmological Physics, University of Chicago, Chicago, IL 60637, USA*

¹¹*National Institute of Standards and Technology, Boulder, CO 80305, USA*

¹²*High-Energy Physics Division, Argonne National Laboratory, Lemont, IL, 60439, USA*

¹³*School of Physics and Astronomy, University of Minnesota, Minneapolis, MN 55455, USA*

¹⁴*Service des Basses Températures, Commissariat à l'Énergie Atomique, 38054 Grenoble, France*

¹⁵*Faculty of Physical Sciences, University of Iceland, 102 Reykjavik, Iceland*

¹⁶*Department of Physics, Harvard University, Cambridge, MA 02138, USA*

¹⁷*Department of Physics, University of Illinois at Urbana-Champaign, Urbana, IL 61801, USA*

¹⁸*Centre for Theoretical Cosmology, DAMTP, University of Cambridge, Cambridge CB3 0WA, UK*

¹⁹*Kavli Institute for Cosmology Cambridge, Cambridge CB3 0HA, UK*

²⁰*Minnesota Institute for Astrophysics, University of Minnesota, Minneapolis, MN 55455, USA*

²¹*Department of Physics, Boston University, Boston, MA 02215, USA*

²²*Department of Physics, University of Chicago, Chicago, IL 60637, USA*

²³*Physics Division, Lawrence Berkeley National Laboratory, Berkeley, CA 94720, USA*

We present the first constraints on multipole-dependent cosmic birefringence using CMB polarization data from the BK18 dataset, which combines observations from BICEP2, Keck Array, and BICEP3 at frequencies of 95, 150, and 220 GHz. Photon coupling to an axion-like field leads to the rotation of CMB polarization, inducing non-zero EB cross-correlations. We show that a multipole-dependent rotation $\beta(\ell)$ imprints a distinct signature in the polarization spectra that can be constrained. Specifically, we consider an Early Dark Energy (EDE) scenario in which a pseudoscalar field couples to photons through a Chern–Simons interaction, generating a polarization rotation with multipole dependence. We introduce a phenomenological $\beta(\ell)$ as a step function, obtaining constraints on the step function size consistent with zero, with uncertainties less than $\sim 0.15^\circ$ (68% CL). In addition, using multi-frequency EE , BB , and EB cross-spectra, along with robust BICEP/Keck foreground treatment and likelihood framework, we derive constraints on the axion–photon coupling amplitude g for several choices of EDE parameters. For the baseline best-fit value $f_{\text{EDE}} = 0.087$ from the *Planck* 2018 analysis, we obtain $g = 0.11 \pm 0.37$ (68% CL), consistent with previous limits.

* dobeck@stanford.edu

† tongtianliu@stanford.edu

I. INTRODUCTION

Cosmic birefringence refers to a rotation of the linear polarization plane of electromagnetic radiation as it propagates through space [1–6]. Such a rotation may arise from a coupling of photons to a pseudoscalar field, as predicted in various extensions of the Standard Model [1, 7–9]. A detection of this effect would provide direct evidence for new physics, such as axion-like particles, which have been proposed as dark matter candidates [9–11].

The Cosmic Microwave Background (CMB) is a particularly sensitive probe of cosmic birefringence [2, 4, 5]. The linear polarization of the CMB can be decomposed into even-parity E -modes and odd-parity B -modes [12–14]. There is no expected correlation between these modes, and the EB cross-spectrum should vanish [15, 16]. A statistically significant detection of a nonzero EB correlation would thus suggest the presence of axion-like fields through Chern–Simons type interactions [2, 17].

Measuring a global rotation is experimentally challenging because it requires knowing the instrumental polarization orientation of each detector with sufficient precision. A uniform per-band effective rotation of an angle α , which results from the aggregate instrumental response of a given frequency band, is degenerate with a global birefringence angle β , such that the observed EB spectrum reflects the sum $\alpha + \beta$ [2, 4]. In this isotropic scenario, the induced EB power spectrum shape is largely proportional to the EE spectrum.

Several strategies have been proposed to break this degeneracy. The BICEP/Keck (BK) collaboration has initiated a dedicated polarization angle calibration campaign [18, 19] to enable forward-modeling constraints on β using known detector angles to measure global birefringence. Alternatively, a new dynamic field can manifest in anisotropic polarization rotation [20, 21] or time-evolving cosmic birefringence [22], which possess distinct signatures that do not require absolute angle calibration to measure. These effects have also been studied in the BK data [23–26]. Another proposed method is to use polarized Galactic dust emission as a calibrator, assuming it produces zero intrinsic EB correlation [5]; however, this assumption has been questioned and demonstrated to be at least partially false [27].

In this paper, we investigate the multipole-dependence (ℓ -dependence) of the rotation angle in BICEP/Keck data. If the pseudoscalar field evolves during recombination, the epoch when CMB polarization was generated, the redshift-dependent rotation will lead to such ℓ -dependence [28, 29]. Since EE modes are generated at different times throughout recombination, a time-varying $\beta(z)$ results in an EB spectrum that encodes the evolving phase structure of the EE peaks. In particular, as the sound horizon changes with redshift, the peaks in the rotated EB spectrum reflect a shifted and temporally smeared version of the original EE peaks [30].

We parameterize this phenomenologically by a multipole-dependent rotation angle function $\beta(\ell)$. Measuring such ℓ -dependence provides a concrete method to distinguish cosmic birefringence from a simple detector rotation [31].

An example of motivated models predicting ℓ -dependent birefringence is *Early Dark Energy* (EDE) [32]. EDE posits a dynamical scalar field that becomes non-negligible around the epoch of matter-radiation equality. The model is characterized by three primary parameters: the maximum fractional energy density f_{EDE} , the critical redshift z_c at which this density is peaked, and the initial field displacement θ_i [33–35]. The field quickly diminishes during recombination from $z \approx 1200$ to $z \approx 900$, leaving minimal impact at late times, and modifies the expansion history in a way that can raise the value of H_0 inferred from the CMB, potentially alleviating the Hubble tension [33, 36, 37].

If the EDE field is a pseudoscalar axion-like particle coupled to electromagnetism via a Chern–Simons interaction, it induces a rotation of CMB polarization. The Lagrangian includes a term that gives rise to this effect:

$$\mathcal{L} \supset -\frac{1}{4}g\phi F_{\mu\nu}\tilde{F}^{\mu\nu}, \quad (1)$$

where g is the axion-photon coupling constant, ϕ is the EDE field, and $\tilde{F}^{\mu\nu}$ is the dual electromagnetic field tensor [1, 10].

The time evolution of ϕ during recombination generates the aforementioned redshift-dependent birefringence angle $\beta(z)$, which leads to an EB spectrum with non-trivial ℓ -dependence [28, 29, 38]. This dependence varies with specific EDE parameters ($f_{\text{EDE}}, z_c, \theta_i$), as shown in Fig. 1 (left). As the EDE fraction f_{EDE} increases, the amplitude of the EB spectrum grows and its peak structure becomes increasingly inconsistent with the shape expected from a constant β . Notably, the corresponding EE spectra remain largely unchanged, indicating that the EB features cannot be adequately captured by a constant rotation angle alone. A 2023 analysis by Eskilt *et al.* [28] searched for this effect using *Planck* polarization data. By comparing the model-predicted EB spectrum to the observed stacked power spectrum, they found $g = 0.04 \pm 0.16$ (68% confidence). While their data did not favor the specific shape predicted by the model, their work demonstrated that the distinct shape of EB can break the α – β degeneracy without requiring absolute calibration or assumptions about Galactic dust [4, 28].

To quantify the difference in shape, we can define an effective rotation angle:

$$\beta(\ell) = \frac{1}{4} \arcsin \left(\frac{2D_\ell^{EB}}{D_\ell^{EE}} \right), \quad (2)$$

which approximates the apparent rotation angle at each ℓ under the assumption that EB arises entirely from rotated EE . This function, shown in Fig. 1 (right) for a representative EDE model, displays the multipole-dependence of the rotation angle that we seek to constrain.

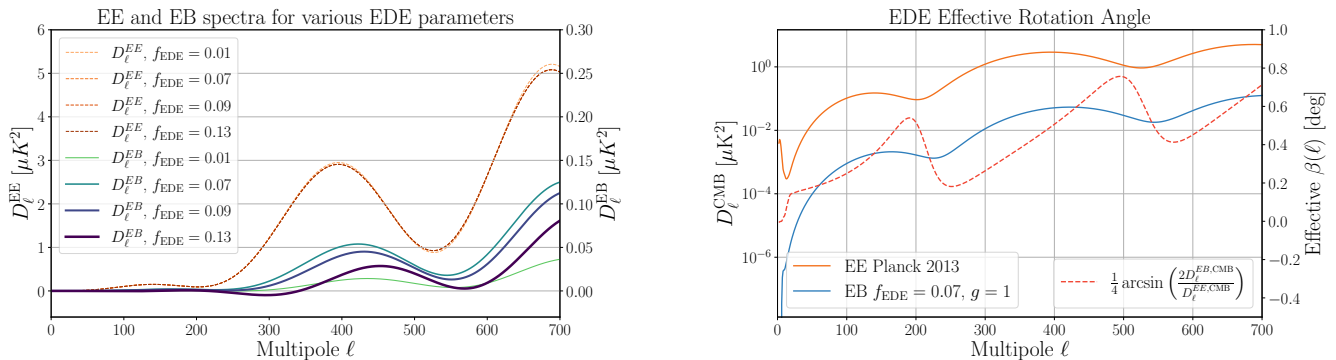


FIG. 1: **Multipole dependence in Early Dark Energy.** (Left) EB and EE spectra generated by Early Dark Energy models with different values of f_{EDE} . As f_{EDE} increases, the EB spectrum (blue) becomes more pronounced and deviates further from a constant rotation model, while the EE spectrum (orange) stays roughly the same. f_{EDE} is the primary driver of these shifts [32, 33, 39], but other parameters (both EDE and standard cosmological parameters) also vary according to best fit values in Table I. Note that EE spectra and EB spectra are on different scales for visual comparison. (Right) Effective rotation angle (red) approximated by $\beta(\ell) = \frac{1}{4} \arcsin(2D_\ell^{EB,CMB}/D_\ell^{EE,CMB})$, where EB (blue) is derived from an EDE model with $f_{\text{EDE}} = 0.07$, and EE (orange) is the best fit curve from *Planck* 2013. Constant-angle models are insufficient for fitting to $\beta(\ell)$.

In this work, we extend the EDE analysis using data from the *BICEP/Keck* Array [18, 40]. While *BICEP/Keck* probes a smaller multipole range ($\ell \lesssim 520$) than *Planck*, its high sensitivity, choice of a clean sky patch, and multi-frequency coverage enable robust measurements of the EB spectrum with low noise and foreground contamination [14, 41].

We present complementary analyses:

1. **Model-independent search for multipole-dependent birefringence** (Section V A): A novel approach modeling $\beta(\ell)$ as a step function, measuring $\Delta\beta = \beta_{\text{low-}\ell} - \beta_{\text{high-}\ell}$ as a signature of multipole-dependent physics independent of any specific EDE model.
2. **EDE model fit** (Section V B): A direct search of EDE-predicted polarization spectra incorporating multicomponent foreground analysis for representative EDE parameters.

Our multipole-dependent approach generalizes previous work by decoupling the analysis from specific EDE models, offering direct sensitivity to a broader range of multipole-dependent physics.

II. DATA MODEL AND LIKELIHOOD

In our analysis, we model the effects of gravitational lensing, isotropic cosmic birefringence, Early Dark Energy (EDE), polarized foregrounds, and effective per-band polarization rotation angles on CMB polarization spectra.

The lensed CMB EE and BB power spectra are computed using *CAMB* [42] with *Planck* 2013 cosmological parameters and no primordial tensor modes [43]. The BB spectrum is scaled by an amplitude parameter A_{lens} to account for uncertainties in the lensing signal:

$$D_\ell^{BB,CMB} = A_{\text{lens}} \cdot D_\ell^{BB,CAMB}. \quad (3)$$

Typically, setting $A_{\text{lens}} = 1$ is sufficient because the BB spectrum has two to three orders of magnitude less impact than EE in constraining rotation from the EB spectrum. However, we allow it to vary when simultaneously fitting the full EE , BB , and EB spectra alongside foreground components. The CMB EB spectrum is modeled as a parity-violating contribution from Early Dark Energy (EDE), calculated with a modified version of *CLASS* [44] developed by Murai *et al.* [29]:

$$D_\ell^{EB,CMB} = g \cdot D_\ell^{EB,EDE}, \quad (4)$$

where g (from Eq. (1)) parametrizes the amplitude of the EDE contribution to the EB spectrum, and $D_\ell^{EB,EDE}$ is the template power spectrum derived from specific EDE parameters. The parameter g has units of M_{pl}^{-1} and is fixed to zero unless explicitly fitting for an EDE signal.

Throughout this work, we denote \tilde{D}_ℓ as rotated CMB spectra, \bar{D}_ℓ as spectra with foregrounds included, and $\bar{\tilde{D}}_\ell$ as spectra after applying per-band rotation angles.

A uniform rotation angle β_{cmb} , representing isotropic cosmic birefringence, is applied to the lensed CMB spectra to obtain the following [16, 45, 46]:

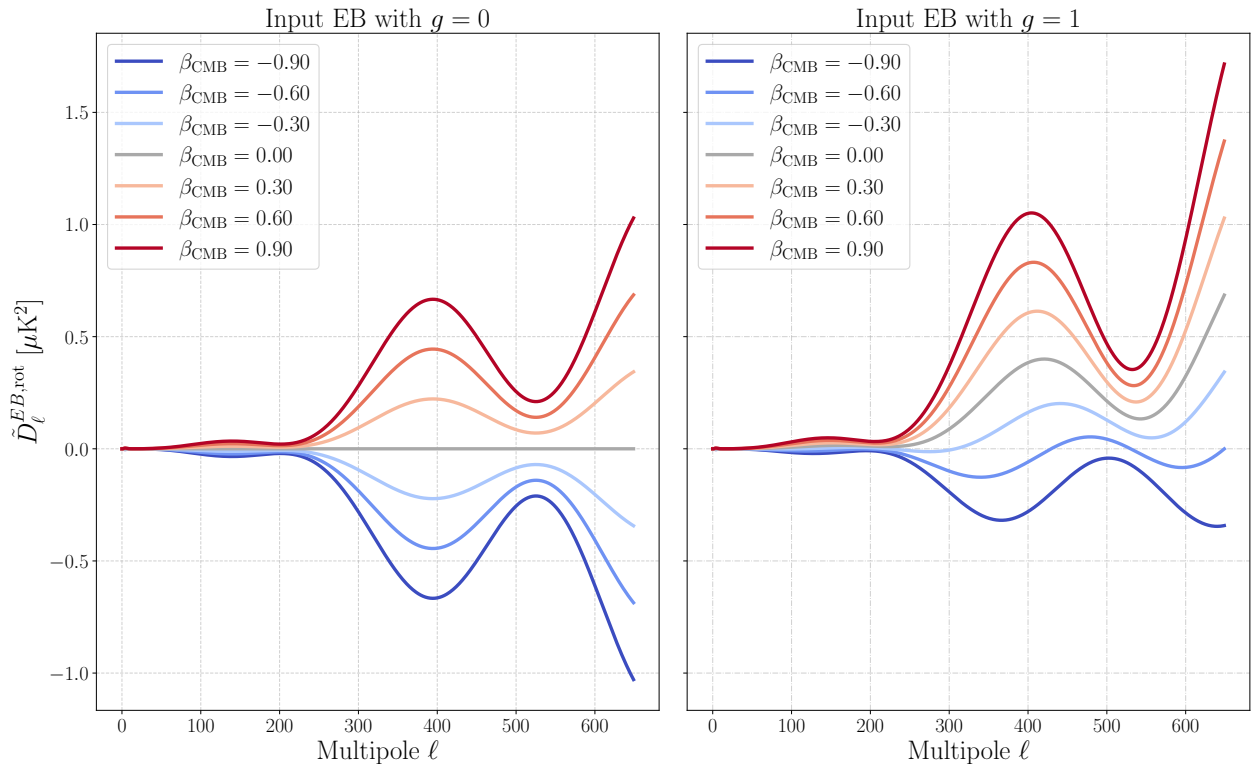


FIG. 2: **Comparison of simulated CMB spectra under isotropic vs. multipole-dependent rotation.** (Left) Standard Λ CDM spectra rotated by different constant angles, β_{cmb} (isotropic birefringence only, $g = 0$). (Right) Spectra including an Early Dark Energy contribution ($g = 1$) rotated by different β_{cmb} . The EDE signal introduces distinct features in the EB spectrum that differ significantly from the isotropic case.

$$\tilde{D}_\ell^{EE,rot} = D_\ell^{EE,CMB} \cos^2(2\beta_{\text{cmb}}) + D_\ell^{BB,CMB} \sin^2(2\beta_{\text{cmb}}) - D_\ell^{EB,CMB} \sin(4\beta_{\text{cmb}}), \quad (5)$$

$$\tilde{D}_\ell^{BB,rot} = D_\ell^{EE,CMB} \sin^2(2\beta_{\text{cmb}}) + D_\ell^{BB,CMB} \cos^2(2\beta_{\text{cmb}}) + D_\ell^{EB,CMB} \sin(4\beta_{\text{cmb}}), \quad (6)$$

$$\tilde{D}_\ell^{EB,rot} = \frac{1}{2} \left(D_\ell^{EE,CMB} - D_\ell^{BB,CMB} \right) \sin(4\beta_{\text{cmb}}) + \frac{D_\ell^{EB,CMB}}{\cos(4\beta_{\text{cmb}})}. \quad (7)$$

Despite the degeneracy between the effective per-band rotation angle α_ν and the isotropic cosmic birefringence angle β_{cmb} , previous measurements have constrained $\beta_{\text{cmb}} \lesssim 1^\circ$ [18]. Thus, the rotation impacts the EB spectrum much more significantly than EE or BB , since EB is approximately linear in both β_{cmb} and g . Sample rotated spectra are illustrated in Figure 2.

When performing the multipole-dependent birefringence analysis, we replace the constant β_{CMB} in Eqs. (5)–(7) with a piecewise-constant model defined by a Heaviside step function at a multipole breakpoint ℓ_b :

$$\beta_{\ell_b}(\ell) = \Delta\beta_{\ell_b} H(\ell - \ell_b), \quad (8)$$

where $\Delta\beta_{\ell_b}$ characterizes the difference in rotation between low- and high- ℓ modes. The birefringence at low

ℓ is not zero, but determined by the per-band rotation angles α_ν such that $\Delta\beta_{\ell_b}$ isolates only the multipole-dependent deviation. We restrict our analysis to this step-function formulation because it allows us to test for multipole-dependence with the minimal increase in model complexity. While more elaborate functional forms for $\beta(\ell)$ could be employed, they introduce additional free parameters that increase the risk of overfitting; a comprehensive study of such models is reserved for future work.

A. Galactic Dust and Synchrotron Treatment

Polarized galactic foregrounds are modeled for each auto- or cross-spectrum XY between frequency bands ν_1 and ν_2 as a sum of dust and synchrotron components:

$$D_\ell^{XY,\text{fg}}(\nu_1 \times \nu_2) = f_d^{\nu_1}(\beta_d, BP^{\nu_1}) \cdot f_d^{\nu_2}(\beta_d, BP^{\nu_2}) \cdot A_d^{XY} \left(\frac{\ell}{\ell_0} \right)^{\alpha_d^{XY}} + f_s^{\nu_1}(\beta_s, BP^{\nu_1}) \cdot f_s^{\nu_2}(\beta_s, BP^{\nu_2}) \cdot A_s^{XY} \left(\frac{\ell}{\ell_0} \right)^{\alpha_s^{XY}}, \quad (9)$$

where $\ell_0 = 80$ is the pivot multipole, and BP^ν denotes the bandpass response function for frequency ν .

The coefficients f_d and f_s capture the scaling of dust and synchrotron power from the pivot frequencies to the actual bandpasses of the maps labeled ν_1 and ν_2 [47].

The foreground contribution is then added to the rotated CMB spectra:

$$\hat{D}_\ell^{XY}(\nu_1 \times \nu_2) = \tilde{D}_\ell^{XY,\text{rot}} + D_\ell^{XY,\text{fg}}(\nu_1 \times \nu_2). \quad (10)$$

As detailed in Section III, this analysis utilizes BICEP/Keck maps at 95, 150, and 220 GHz. At these frequencies, the synchrotron signal is negligible relative to thermal dust. We therefore fix the dust-synchrotron correlation parameter to zero, as the data lack the sensitivity required to meaningfully constrain this term [40].

B. Per-Band Angle Rotation

We apply a per-band polarization angle rotation α_ν as an additional rotation on the spectra after including foreground contributions. This per-band rotation models the contributions from instrumental sources.

$$\begin{aligned} \bar{D}_\ell^{EE}(\nu_1 \times \nu_2) &= \hat{D}_\ell^{EE}(\nu_1 \times \nu_2) \cos(2\alpha_{\nu_1}) \cos(2\alpha_{\nu_2}) + \hat{D}_\ell^{BB}(\nu_1 \times \nu_2) \sin(2\alpha_{\nu_1}) \sin(2\alpha_{\nu_2}) \\ &\quad - \hat{D}_\ell^{EB}(\nu_1 \times \nu_2) \cos(2\alpha_{\nu_1}) \sin(2\alpha_{\nu_2}) - \hat{D}_\ell^{BE}(\nu_1 \times \nu_2) \sin(2\alpha_{\nu_1}) \cos(2\alpha_{\nu_2}), \end{aligned} \quad (11)$$

$$\begin{aligned} \bar{D}_\ell^{BB}(\nu_1 \times \nu_2) &= \hat{D}_\ell^{EE}(\nu_1 \times \nu_2) \sin(2\alpha_{\nu_1}) \sin(2\alpha_{\nu_2}) + \hat{D}_\ell^{BB}(\nu_1 \times \nu_2) \cos(2\alpha_{\nu_1}) \cos(2\alpha_{\nu_2}) \\ &\quad + \hat{D}_\ell^{EB}(\nu_1 \times \nu_2) \sin(2\alpha_{\nu_1}) \cos(2\alpha_{\nu_2}) + \hat{D}_\ell^{BE}(\nu_1 \times \nu_2) \cos(2\alpha_{\nu_1}) \sin(2\alpha_{\nu_2}), \end{aligned} \quad (12)$$

$$\begin{aligned} \bar{D}_\ell^{EB}(\nu_1 \times \nu_2) &= \hat{D}_\ell^{EE}(\nu_1 \times \nu_2) \cos(2\alpha_{\nu_1}) \sin(2\alpha_{\nu_2}) - \hat{D}_\ell^{BB}(\nu_1 \times \nu_2) \sin(2\alpha_{\nu_1}) \cos(2\alpha_{\nu_2}) \\ &\quad + \hat{D}_\ell^{EB}(\nu_1 \times \nu_2) \cos(2\alpha_{\nu_1}) \cos(2\alpha_{\nu_2}) - \hat{D}_\ell^{BE}(\nu_1 \times \nu_2) \sin(2\alpha_{\nu_1}) \sin(2\alpha_{\nu_2}), \end{aligned} \quad (13)$$

$$\begin{aligned} \bar{D}_\ell^{BE}(\nu_1 \times \nu_2) &= \hat{D}_\ell^{EE}(\nu_1 \times \nu_2) \sin(2\alpha_{\nu_1}) \cos(2\alpha_{\nu_2}) - \hat{D}_\ell^{BB}(\nu_1 \times \nu_2) \cos(2\alpha_{\nu_1}) \sin(2\alpha_{\nu_2}) \\ &\quad - \hat{D}_\ell^{EB}(\nu_1 \times \nu_2) \sin(2\alpha_{\nu_1}) \sin(2\alpha_{\nu_2}) + \hat{D}_\ell^{BE}(\nu_1 \times \nu_2) \cos(2\alpha_{\nu_1}) \cos(2\alpha_{\nu_2}). \end{aligned} \quad (14)$$

C. Band Power Window Functions

To directly compare theoretical model spectra with observational data, each theoretical auto- or cross-spectrum $\bar{D}_\ell^{XY}(\nu_1 \times \nu_2)$ is convolved with the corresponding bandpower window functions (BPWFs), computed as

$$D_b^{XY}(\nu_1 \times \nu_2) = \sum_\ell W_{b\ell} \bar{D}_\ell^{XY}(\nu_1 \times \nu_2), \quad (15)$$

where b indexes the bandpower and $W_{b\ell}$ is the weight assigned to multipole ℓ . This convolution effectively bins the theory spectra into the same format as the data, incorporating deprojection, filtering, weighting, and instrumental filtering effects applied during data processing [14]. For the EB cross-spectrum, we approximate the window functions as the geometric mean of the EE and BB functions. While this approximation is known to introduce a multiplicative bias of a few percent [18], this effect is negligible for our analysis given that the target birefringence signals are small and the uncertainty bud-

get is dominated by statistical noise.

Each BPWF characterizes how power at multipole ℓ contributes to a given multipole band, typically peaking near the band center and tapering toward adjacent bands (Figure S2a). While each bandpower receives contributions from a range of multipoles, the band edges, defined as the midpoint between adjacent band centers, encompass the range of dominant contributions. These band edges guide the choice of ℓ_b breakpoints used to capture multipole-dependent birefringence.

Figures S2c and S2d illustrate the effect of applying the BPWF convolution on EB spectra, highlighting changes for varying parameters g and dust foregrounds, respectively. Our analysis uses bandpowers corresponding to the multipole range $20 \lesssim \ell \lesssim 520$.

D. Likelihood Calculation

For all auto- and cross-spectra XY and frequency pairs (ν_1, ν_2) , the binned bandpowers are concatenated to form the model prediction vector:

$$\mathbf{D}^{\text{model}}(\Theta) = \bigoplus_{XY, \nu_1, \nu_2} \left[D_{b,1}^{XY}(\nu_1 \times \nu_2), \dots, D_{b, N_{\text{spec}}}^{XY}(\nu_1 \times \nu_2) \right], \quad (16)$$

where N_{spec} is the total number of E and B power spectra that are chosen to be included into the likelihood calculation. This stacking matches the structure of the observed data vector \mathbf{D}^{data} , enabling direct likelihood evaluation. The Gaussian log-likelihood is then evaluated as:

$$-2 \ln \mathcal{L} = (\mathbf{D}^{\text{model}}(\Theta) - \mathbf{D}^{\text{data}})^T \boldsymbol{\Sigma}^{-1} (\mathbf{D}^{\text{model}}(\Theta) - \mathbf{D}^{\text{data}}) \quad (17)$$

where $\boldsymbol{\Sigma}$ is the bandpower covariance matrix. We use the same bandpower covariance matrix as previous analyses [14], where it is estimated using the baseline 499 simulations. To improve stability, terms with zero expected covariance are explicitly set to zero to reduce the noise from the finite number of simulated realizations.

We use a Gaussian likelihood for computational efficiency and consistency with previous birefringence analyses. Given that the constraining power in our analysis focuses primarily on intermediate multipoles $\ell \sim 300\text{--}500$, the differences from the Hamimeche–Lewis likelihood are negligible for the parameter constraints presented here.

In summary, the sampled model parameter set is:

$$\Theta = \left\{ \begin{array}{l} \beta_{\text{cmb}}, \quad A_{\text{lens}}, \quad g, \quad \{\alpha_\nu\}, \\ \{A_d^{XY}, \alpha_d^{XY}\}, \quad \{A_s^{XY}, \alpha_s^{XY}\}, \\ \beta_s, \quad \beta_d \end{array} \right\}, \quad (18)$$

where:

- α_ν are the per-frequency effective rotation angle parameters, used in Eqs. (11)–(14).
- β_{cmb} is the isotropic cosmic birefringence angle.
 - In model-independent birefringence runs, β_{cmb} is modeled as a step function by substituting Eq. (8) into Eqs. (5)–(7).
 - In EDE analyses, β_{cmb} is set to zero, so the α_ν 's become the overall per-band polarization rotation angle, whether from instrumentation or cosmological origin.
- g is the photon-axion coupling constant that parametrizes parity-violating interactions in Early Dark Energy models (Eq. (4)). It is set to zero when EDE is not included.
- A_{lens} controls the amplitude of lensing in the BB spectrum. This parameter allows for variations in the lensing amplitude to account for uncertainties in the lensing measurement (Eq. (3)).

- A^{XY} and α_{XY} denote the amplitude and spectral tilt parameters for foreground components (dust and synchrotron) for each polarization spectrum type $XY \in \{EE, BB, EB\}$. The spectral indices β_s and β_d describe the frequency dependence of synchrotron and dust emission, respectively. Used in Eqs. (9)–(10).

In this analysis, we do not treat the EDE fraction f_{EDE} as a free parameter; attempting to simultaneously constrain f_{EDE} can introduce volume effects [33]. Furthermore, because the EE power exceeds the BB and EB power by orders of magnitude, the EE spectrum is effectively insensitive to the small rotations induced by birefringence. Consequently, we fix the background EDE parameters, which are primarily sensitive to TT , EE , and TE [48], and instead adopt representative scenarios with f_{EDE} values motivated by prior literature: 0.012 (ACT), 0.07 (Planck), 0.087 (Planck + BOSS), and 0.127 (Planck + BOSS + SH0ES) [28, 29, 33, 49] when fitting for the photon-axion coupling constant g .

We perform the Markov Chain Monte Carlo (MCMC) analysis using the *Cobaya* framework [50], imposing flat priors on all parameters with ranges chosen to be significantly wider than the expected posterior constraints. We verified that the posterior distributions for all sampled parameters are well-contained within the prior ranges, with negligible probability density at the unphysical boundaries. Flexible configurations allow fixing subsets of parameters or data cuts (e.g., setting EB foregrounds to zero or excluding EE and BB spectra) to isolate specific effects. Convergence is assessed via the Gelman–Rubin statistic [51] $R - 1 < 0.01$ (or < 0.005 when foreground amplitudes are fixed). These criteria follow the standards established by Dunkley *et al.* [52], ensuring that sampling errors in the posterior distribution are negligible compared to statistical uncertainties.

Parameter constraints are derived from marginalized posterior distributions. We marginalize over all α_ν in our real results. Since this work primarily searches for a multipole-dependent effect, this marginalization will not affect the constraining power. We reserve the full discussion of the EB spectra and their best fit α_ν for future work.

III. DATA AND SIMULATIONS

The data used in this analysis come from the *Planck* Satellite [53] and the BICEP/*Keck* data through the 2018 observing season (BK18) [40]. BK18 is a compilation of observations by the BICEP2, *Keck* Array, and BICEP3 telescopes at the South Pole. The high-altitude, dry, and stable environment enables deep integration on small patches of the sky with minimal atmospheric interference, making it ideal for precise measurements of CMB polarization. Previous analysis of BK18 yielded a constraint on inflationary B -modes of $r < 0.036$ at 95% confidence [40].

A. BK18 Dataset

The BK18 dataset includes observations from three generations of instruments:

- **BICEP2:** A 150 GHz receiver operated from 2010 to 2012, utilizing approximately 500 bolometers [14].
- **Keck Array:** Operated from 2012 to 2019, initially with five 150 GHz receivers, later expanded to include 95 and 220 GHz receivers [40].
- **BICEP3:** A receiver observing at 95 GHz, operational since 2016 with roughly 2500 bolometers [40].

The combined data cover an effective sky area of approximately 400 square degrees for BICEP2 and *Keck* Array, and up to 600 square degrees for BICEP3. Maps employ an equirectangular pixelization with $0.25^\circ \times 0.25^\circ$ pixels. Observations target a region centered at RA = 0h, Dec = -57.5° [18].

Maps are constructed per observation phase after filtering time-ordered data. This process includes the removal of third-order polynomial trends, filtering of scan-synchronous signals, and removal of beam systematics by deprojection [40]. Weighting is applied using inverse noise variance derived from the timestreams, yielding estimates of the Stokes parameters T, Q, U and their variances. The Q and U maps are converted to E and B using a map-based purification method described in BK-VII [54].

A suite of jackknife null tests is performed to validate data quality and identify systematic contamination [14]. In this work we use additional multipole bandpowers compared to the standard BK18 analysis to achieve stronger constraining power. We verify that these higher multipole bandpowers pass the standard suite of jackknife tests. Following the procedure described in Appendix B of BK-XIII [40], we repeat all χ^2 and χ null tests using the same data-split definitions but extend the number of bandpowers from the baseline nine to fourteen, so that we use multipoles up to $\ell \approx 520$.

We find that the distribution of Probability to Exceed (PTE) values remains consistent with expectations from simulations (Figure 3), with no increase in the number of extreme PTEs (< 0.01 or > 0.99) relative to the baseline analysis for any of the map frequencies.

We analyze the four mapsets of BK18: the large-field 95 GHz maps and three small-field maps at 95 GHz, 150 GHz and 220 GHz. We also use external *Planck* data, namely the PR4 maps at 30 GHz, 44 GHz, 143 GHz, 217 GHz and 353 GHz [53], to constrain foreground parameters, particularly thermal dust, which dominates at higher frequencies. By marginalizing over foregrounds, we effectively separate their contribution from the cosmological signal.

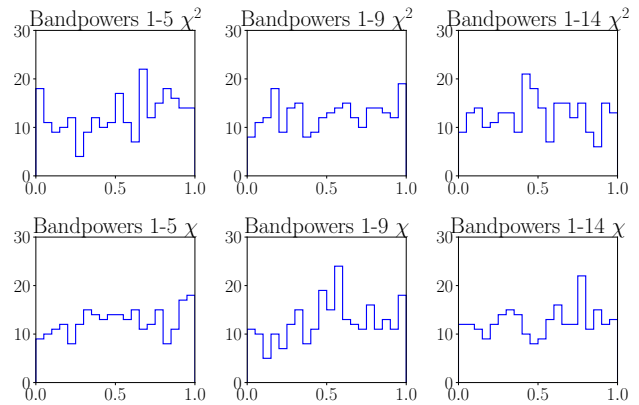


FIG. 3: Distributions of the jackknife χ^2 and χ PTE values for the Keck Array 2016, 2017, and 2018 220 GHz data. This figure is analogous to Fig. 12 of BKXIII [40], but with an additional rightmost column showing the extended multipole range (bandpowers 1–14), explicitly checking that the higher multipole bandpowers also satisfy the jackknife consistency criteria.

B. Simulations

To characterize systematics, validate estimators, and compute uncertainties, we create realistic simulations of the observed data. We follow the standard procedure in the BICEP/*Keck* power-spectrum analysis, with steps summarized below. See Refs. [14, 54, 55] for further methodological details.

We construct two simulation sets, both using the standard BICEP/*Keck* CMB and Gaussian dust modeling for simulating maps. The sets consist of 499 realizations processed through the full BICEP/*Keck* power-spectrum-estimation pipeline. The only difference is the inclusion of an EDE-induced EB signal in one of the two datasets:

- **baseline:** These are the simulations used in the main BK18 analysis. They contain a lensed Λ CDM signal, sign-flip noise, and foreground dust, with no injected birefringence signal ($g = 0$).
- **EDE:** These are identical to the **baseline** simulations but with a EB signal injected into the input spectra. This signal is generated by an Early Dark Energy model with $f_{\text{EDE}} = 0.07$ and $g = 1$ (Table I). The parameter f_{EDE} represents the peak fraction of Early Dark Energy during recombination, with the chosen value taken from the best-fit *Planck* model in Murai *et al.* [29].

The simulation pipeline involves several steps. We first generate full-sky signal-only realizations of the CMB sky sampling from theoretical power spectra derived from *Planck* best-fit parameters. We then beam-convolve and reobserve the full-sky maps [54], encoding the real instrument’s scan strategy and time-domain filtering, to

produce maps that reflect the actual sky coverage and resolution of the experiment.

Instrumental noise is added next. Noise realizations are derived from sign-flip simulations, created by randomly flipping the sign of real data subsets. This method preserves the statistical properties of the noise while suppressing the sky signal. We also include simulated foreground dust emission, which is modeled as Gaussian realizations drawn from an analytic power spectrum with parameters informed by *Planck* observations. These realizations are scaled across frequencies using a modified blackbody spectrum.

After combining signal, noise, and dust, the maps undergo purification to reduce *E*-to-*B* leakage [54]. A purification matrix projects out ambiguous modes. Power spectra are then estimated using a ring-annulus Fourier estimator, which computes two-point correlations in annular bins in multipole space. This yields bandpower estimates for the *EE*, *BB*, and *EB* spectra.

The power spectra are computed in 14 multipole bandpowers spanning $\ell = 20$ to 520, extending beyond the multipole range of $20 \lesssim \ell \lesssim 355$ used in the *BB* analysis to increase sensitivity to multipole-dependent birefringence signatures.

IV. PIPELINE VALIDATION

We validate our two pipelines for constraining phenomenological multipole dependence and specific Early Dark Energy models using realistic simulations introduced in Section III B.

A. Estimator for Recovering Multipole-Dependent Step-Function

We validate our estimator for multipole-dependent polarization rotation, modeled as a step function in $\beta(\ell)$, using our two simulation datasets: **baseline** and **EDE**. This approach introduces a single new parameter $\Delta\beta_{\ell_b}$, minimizing the total number of free parameters in our MCMC run.

We fix the axion-photon coupling $g = 0$ and set all foreground amplitudes to zero so that all the multipole-dependence is captured by the step-function. We use only the *EB* cross-spectra in the data vector and fit for the four BK per-band polarization rotation angle parameters α_ν and the step amplitude $\Delta\beta_{\ell_b}$. The multipole breakpoints $\ell_b = 265, 300, 335, 370, 405$ correspond approximately to the band edges near the second peak of the *EE* spectrum.

Low values of ℓ_b may not capture the EDE-induced signal concentrated near the *EE* peak, while high values reduce constraining power due to fewer high- ℓ bandpowers. The selected values strike a balance between these effects while leaving room for signals induced by models other than our specific EDE parameter set.

For each ℓ_b , we run MCMC chains on all 499 realizations in both simulation sets, using a convergence criterion of $R-1 < 0.03$. From each realization's marginalized 1D posterior, we extract the mean value of $\Delta\beta_{\ell_b}$ to serve as a single estimate. We then treat these 499 individual estimates as a new distribution to validate the estimator's performance. As shown in Table S1, the ensemble average and 68% credible interval of these 499 estimates are consistent with the null result in the **baseline** simulations; the recovered $\Delta\beta_{\ell_b}$ values are consistent with zero across all breakpoints, as expected. In contrast, for the **EDE** simulations, the distribution of recovered $\Delta\beta_{\ell_b}$ exhibits a $1-2\sigma$ level shift, consistent with the ℓ -dependent signal predicted by the EDE model (Figure S1).

The mean values and 68% credible intervals across all tested ℓ_b are summarized in Table S1 and plotted in Figure S3b for comparison. We find that the 68% credible interval on $\Delta\beta_{\ell_b}$ is between 0.1° – 0.2° over the angular scale to which we are sensitive. These validation results are within our expectations and demonstrate our sensitivity to multipole-dependence.

B. Estimator for Recovering EDE photon-axion coupling

To assess the robustness of our inference pipeline in recovering the photon-axion coupling constant g , we carry out an extensive suite of validation tests using the two simulation datasets: **baseline** and **EDE**. We explore a range of EDE scenarios, foreground configurations, and injected per-band rotation signals. Our goal is to determine whether the pipeline can reliably recover the injected coupling parameter g and the polarization rotation angles α_ν for each frequency band.

As explained in Section II D, we do not fit for the EDE fraction f_{EDE} ; instead, we choose a representative set of fiducial EDE parameters described in Table I.

1. Impact of Different Polarization Cross-Spectra

Our MCMC likelihood supports fitting to different combinations of polarization spectra:

- Marginalizing over foregrounds, free A_s and A_d :
 - *EE* + *EB*
 - *EE* + *EB* + *BB* (A_{lens} fixed to 1)
 - *EE* + *EB* + *BB* (free A_{lens})
- Without marginalizing over foregrounds, A_s and A_d set to zero:
 - *EB*-only

For each test configuration, we run the pipeline on all 499 simulations, using the mean of each posterior as the best-fit value. We then compile the best-fit values from

TABLE I: **Best-fit cosmological parameters for Early Dark Energy (EDE) models** based on ACT and *Planck* datasets, compiled from [36, 39]. The ACT-motivated EDE0.012 benchmark corresponds to a minimal EDE fraction, while *Planck*-based fits span a wider range of f_{EDE} values up to 0.127. These parameters are used to generate the *EB* spectra shown in Fig. 1.

Parameter	ACT (EDE0.012)	<i>Planck</i> (EDE0.07)	<i>Planck</i> +BOSS (EDE0.087)	<i>Planck</i> +BOSS+SH0ES (EDE0.127)
$100\omega_b$	2.233	2.259	2.266	2.276
ω_{cdm}	0.1198	0.1268	0.1285	0.1328
$100 \times \theta_s$	1.041	1.041	1.041	1.041
$\ln(10^{10} A_s)$	3.043	3.058	3.063	3.068
n_s	0.965	0.9789	0.9833	0.9916
τ_{reio}	0.054	0.0549	0.0563	0.0555
f_{EDE}	0.012	0.070	0.087	0.127
$\log_{10} z_c$	3.500	3.563	3.559	3.562
$\theta_{i,\text{scf}}$	2.749	2.742	2.747	2.761

all realizations and compare them to the contours from a single realization; a comparable shape validates the predicted uncertainty (Figure S4). We find unbiased recovery of the sampled parameters.

For the **baseline** simulation set (null birefringence), the recovered values of g and α_ν are consistent with zero across all tested configurations (Table S2), demonstrating the accuracy and precision of the estimator in the absence of a birefringent signal. The 68% credible interval on g ranges from 0.31 to 0.40.

For the **EDE** set, using only *EB* and *EE* spectra yields unbiased recovery of both g and α_ν (Table S3). However, when *BB* spectra are included with A_{lens} fixed to 1, we observe a suppression in the recovered g values and an increase of α_ν . The likelihood compensates for a *BB* mismatch by shifting the effective per-band rotation angles α_ν . Due to parameter correlations, this inflation of α_ν leads to a corresponding suppression in g . This suppression suggests an inconsistency between the model and the simulation *BB* lensing amplitude, which is also reflective of the existing uncertainties in the *Planck* lensing models [56]. Allowing A_{lens} to float significantly mitigates this bias and restores parameter recovery to expected values.

2. Impact of EDE Parameters Used in Generating the *EB* Curve

We also examine how the recovered polarization rotation angles α_ν and coupling g vary as a function of the *EB* template $D_\ell^{\text{EB,EDE}}$ used in the likelihood, under both $g = 0$ and $g = 1$ simulation scenarios. We use a modified version of CLASS [44] developed by Murai *et al.* [29] to generate four different $D_\ell^{\text{EB,EDE}}$ curves using the EDE parameters described in Table I. We then run the MCMC pipeline for each *EB* template across all 499 simulations for both **baseline** and **EDE**. The **EDE** sims, including the injected f_{EDE} value, stay the same. Only the *EB* cross-spectra are included in this likelihood calculation. Since *EE* and *BB* are dominated by standard cosmology and foregrounds, this restriction allows

us to isolate the dependence of our recovered parameters on the specific EDE template shape without introducing unnecessary covariance.

For the **baseline** simulation set (Table S2), the recovered g and α_ν parameters are consistent with zero in all cases, demonstrating that the estimator remains unbiased regardless of the assumed EDE model used to construct $D_\ell^{\text{EB,EDE}}$. However, for the case where $f_{\text{EDE}} = 0.012$, the bias and uncertainty of g increases. This occurs because the induced signal in $D_\ell^{\text{EB,EDE}}$ is small for these parameters, making it more difficult to break the degeneracy between EDE-induced birefringence and effective per-band rotation.

In the **EDE** simulation set (Table S3), where the signal is injected at $g = 1$, the recovered parameters show mild bias depending on the choice of *EB* template. This is expected: the injected $D_\ell^{\text{EB,injected}}$ in EDE corresponds to a specific set of EDE parameters where $f_{\text{EDE}} = 0.07$, while the $D_\ell^{\text{EB,EDE}}$ used in the validation do not match for the remaining 3 of the 4 parameter sets. When the template does not match the injected signal, the likelihood fit can yield biased estimates.

This highlights the limitations of assuming a fixed functional form for the Early Dark Energy signal. Since the true EDE parameters are not precisely known and are subject to change with future observations, this introduces systematic uncertainty into the inference of g . These results motivate the multipole-dependent approach described in Section VA, which allows for more flexible recovery of birefringence without assuming a specific EDE model. Nevertheless, we find that the *EB*-only analysis remains sensitive to birefringence effects at the tested coupling scale.

3. Impact of Different Dust Models

We run the MCMC pipeline on multiple datasets using a variety of dust models to assess the impact of foreground modeling on the estimator's recovery of g . The **baseline** dataset uses a Gaussian dust model for fore-

grounds in the BICEP/Keck patch. To test robustness, we repeat the analysis using several alternative dust realizations. See Ref. [40] for detailed descriptions of each model.

Across all cases, fitting jointly to EE , BB , and EB spectra, the estimator consistently recovers values of g consistent with zero (Table S5). The recovered values show minimal variation between models, indicating that foreground modeling does not significantly bias our constraints on g .

4. Impact of Injected Per-Band Rotation

To validate the robustness of our estimator against isotropic per-band rotation from instrumental sources, we inject known polarization rotation angles directly into the EB spectra. This test evaluates whether the estimator can recover rotation angles correctly without biasing the inference of the photon-axion coupling parameter g .

We test three configurations of injected rotation angles across the four frequency bands (Table S6). For each configuration, we compute the corresponding theoretical EB spectra, $\bar{D}_\ell^{EB, \text{injected}}(\nu_1 \times \nu_2)$, convolve them with the Band Power Window Functions (BPWFs), and add the resulting bandpowers to each realization in both the **baseline** and **EDE** datasets. Foregrounds and isotropic birefringence (β_{cmb}) are set to zero in the likelihood model for this test. This simplification allows us to isolate the estimator's response to the injected rotation angles without introducing unnecessary covariance from foreground marginalization or cosmological parameter degeneracies.

The MCMC pipeline is then executed for each injected rotation scenario. The injected rotation angles are accurately recovered without introducing bias in the recovered g (Table S6). Specifically, for both **baseline** and **EDE** simulation sets, the estimated g remains consistent with the input value regardless of the rotation angle pattern. This test confirms that the estimator can distinguish between detector rotation-induced EB and EDE-induced EB and indicates that per-band rotation does not lead to artificial suppression or increase of the EDE signal.

V. RESULTS

A. Constraints on Multipole-Dependent Birefringence

At each ℓ_b , we perform a Markov Chain Monte Carlo (MCMC) analysis jointly fitting the four BK18 per-band rotation angles α_ν and a single $\Delta\beta_{\ell_b}$. All chains satisfy the convergence criterion $R - 1 < 0.005$.

Fitting to the real BK18 data with the estimator validated in Section IV A, Table II shows best-fit values for the $\beta(\ell)$ function at each ℓ breakpoint. In all cases, the

data prefer values of $\Delta\beta_{\ell_b}$ consistent with zero at $\leq 1\sigma$, and no statistically significant deviations are observed.

TABLE II: **Step Function Constraints.** Posterior mean and 68% credible intervals for the multipole-dependent rotation angle step $\Delta\beta_{\ell_b}$ at each multipole breakpoint. The step-function model enables sensitivity to multipole-dependent rotation by splitting low- and high- ℓ bandpowers.

Breakpoint (ℓ_b)	Size of Angle Difference ($\Delta\beta_{\ell_b}$) (deg)
265	-0.15 ± 0.15
300	-0.01 ± 0.14
335	0.05 ± 0.13
370	0.11 ± 0.13
405	0.09 ± 0.15

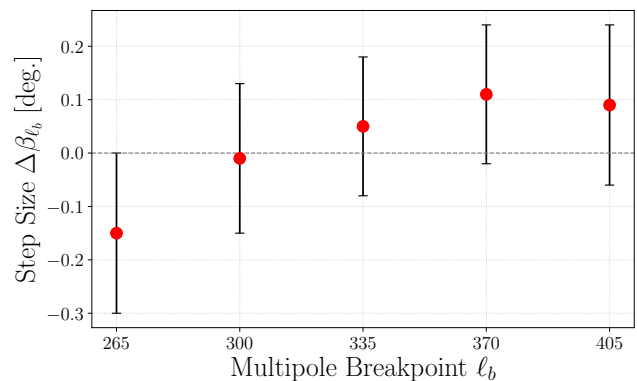


FIG. 4: **Step Function Constraints.** Best-fit $\beta(\ell)$ step function for five values of the ℓ_b breakpoints with 1σ uncertainty. All values are consistent with $\Delta\beta_{\ell_b} = 0$.

These results provide the first model-independent constraints on multipole-dependent birefringence from BICEP/Keck data. They demonstrate the viability of CMB polarization spectra to probe time-varying parity-violating physics without strong assumptions about the underlying dynamics.

B. Constraints on Early Dark Energy

We perform an extension to the analysis by Eskilt *et al.* [28] using BICEP/Keck data, as well as the *Planck* spectra. In addition to EB -only fits, our analysis includes the EE and BB spectra and marginalizes over synchrotron and dust templates as described in Section II, allowing for more robust constraints that account for potential foreground contamination.

We apply the same estimator validated in Section IV B to real BK18 data, sampling over g for each fixed value of f_{EDE} .

Posterior distributions for g are consistent with zero across all f_{EDE} values, as summarized in Table III. The

TABLE III: **EDE Constraints.** Posterior mean and 68% credible intervals on the photon-axion coupling g (units of M_{pl}^{-1}) at fixed EDE parameter values across multiple analysis configurations and data subsets.

Data in Likelihood	$f_{\text{EDE}} = 0.012$	0.070	0.087	0.127
Eskilt-only	0.05 ± 0.44	0.05 ± 0.18	0.03 ± 0.16	0.03 ± 0.13
BK18 EB-only	0.48 ± 0.99	0.20 ± 0.46	0.21 ± 0.39	0.23 ± 0.30
BK18 EE+EB	0.41 ± 1.01	0.12 ± 0.41	0.14 ± 0.38	0.17 ± 0.31
BK18 EE+EB+BB	0.28 ± 1.01	0.07 ± 0.40	0.11 ± 0.37	0.11 ± 0.31
BK18 EE+EB+BB free A_{lens}	0.21 ± 1.02	0.06 ± 0.43	0.08 ± 0.37	0.10 ± 0.31

baseline result using Eskilt’s baseline EDE parameters is shown in Fig. 5. Marginalizing over foreground parameters does not significantly change the central values or widths of the posteriors, confirming the robustness of our constraints.

For the baseline EDE parameters ($f_{\text{EDE}} = 0.087$), Eskilt *et al.* [28] reported a constraint of $g = 0.04 \pm 0.16$ using *Planck* and BOSS data. For the same EDE parameters, our most robust configuration (EE+EB+BB) yields $g = 0.11 \pm 0.37$. While consistent with the *Planck* result, our uncertainty is approximately a factor of 2 larger. This difference in our sensitivity reflects the trade-off between the full-sky coverage of *Planck*, which accesses a wider range of multipoles, and the deep, focused integration of BICEP/*Keck* on a smaller patch of sky.

Notably, the tightest constraints occur at higher f_{EDE} , where the EDE-induced *EB* templates deviate more significantly from a simple rotated *EE* spectrum. The tighter constraints indicate stronger evidence against large signals of EDE, especially in multipole ranges sensitive to the time evolution of birefringence. Because of the limited sky coverage and angular resolution, the spectra from BICEP/*Keck* data have a limited multipole range, limiting their statistical power compared to full-sky missions.

VI. CONCLUSION

We have presented the first constraints on multipole-dependent cosmic birefringence using *EB* power spectra from BICEP/*Keck*. Parity-violating Early Dark Energy models serve as a compelling theoretical test case, offering a physically motivated example of ℓ -dependent effects in the early universe.

To probe multipole-dependent effects, we introduced the phenomenological parameter $\Delta\beta_{\ell_b}$, describing a step-like change in rotation angle at multipole ℓ_b . Across the tested range of breakpoints, $\Delta\beta_{\ell_b}$ was consistent with zero within uncertainties of $\sim 0.15^\circ$, placing the first phenomenological limits on a time-evolving parity-violating field during recombination.

We further constrained an axion-like EDE model with Chern–Simons coupling to photons, placing bounds on the axion-photon coupling g for benchmark EDE parameters with varying energy fractions f_{EDE} . Using BK18 data with multicomponent frequency coverage and ro-

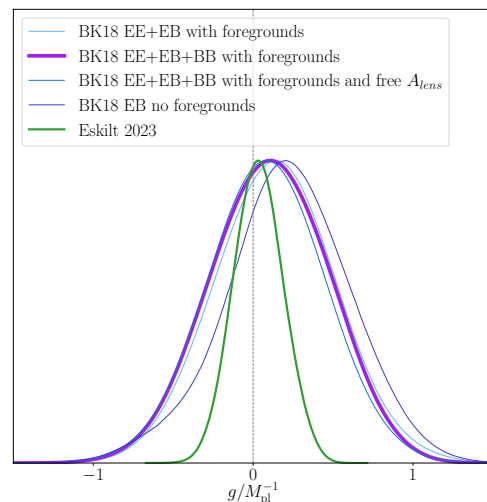


FIG. 5: **EDE Constraints.** Posterior distribution on the axion-photon coupling g from BK18 (this work), overlaid with the constraint from *Planck* EB analysis by Eskilt *et al.* [28] with the EDE parameters from their baseline result.

bust foreground marginalization, we found the results to be consistent with the null hypothesis and to agree with existing limits from *Planck*.

Importantly, this work establishes a versatile framework for testing multipole-dependent cosmic birefringence with CMB polarization, where more flexible parameterizations of $\beta(\ell)$ could be explored in future work. While we avoided models requiring more than one free parameter for this work, modeling the rotation angle as a linear or periodic function of ℓ would allow for a wider class of multipole-dependent effects with only modest increases in model complexity. However, such extensions must be approached with care to avoid overfitting in the absence of strong theoretical priors. Incorporating foregrounds and other polarization spectra directly into the $\beta(\ell)$ analysis framework is another natural extension.

Future calibration campaigns for BICEP3 are expected to yield precise measurements of absolute polarization angles, which are currently unconstrained in this analysis. As detailed in BICEP/*Keck* XVIII [18], establishing these absolute reference angles will break the degeneracy between isotropic cosmic birefringence and instrumental

rotation. This advancement will enable direct constraints on β_{cmb} and significantly improve the separation of cosmological signals from instrumental systematics.

ACKNOWLEDGMENTS

The BICEP/Keck projects have been made possible through a series of grants from the National Science Foundation, most recently including 2220444–2220448, 2216223, 1836010, and 1726917. The development of antenna-coupled detector technology was supported by the JPL Research and Technology Development Fund and by NASA Grants 06-ARPA206-0040, 10-SAT10-0017, 12-SAT12-0031, 14-SAT14-0009, and 16-SAT-16-0002.

The development and testing of focal planes was supported by the Gordon and Betty Moore Foundation at Caltech. Readout electronics were supported by a

Canada Foundation for Innovation grant to UBC. Support for quasi-optical filtering was provided by UK STFC grant ST/N000706/1. The computations in this paper were run on the Odyssey/Cannon cluster supported by the FAS Science Division Research Computing Group at Harvard University. The analysis effort at Stanford and SLAC is partially supported by the U.S. DOE Office of Science.

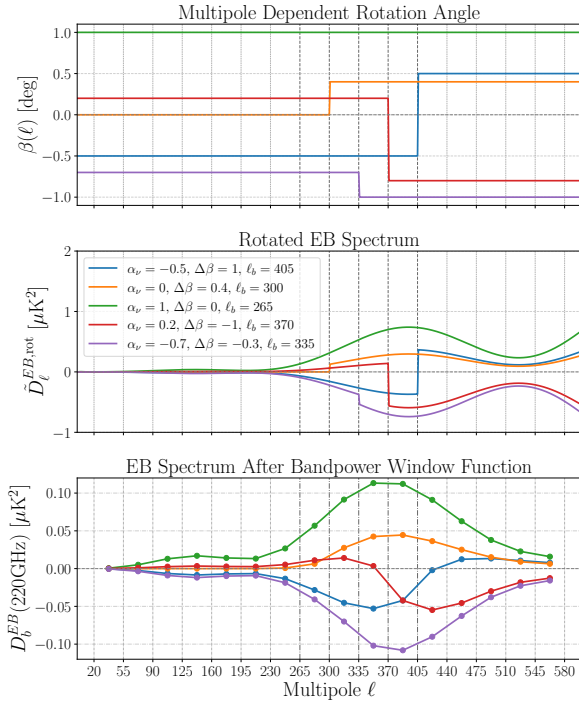
We thank the staff of the U.S. Antarctic Program and in particular the South Pole Station, without whose help this research would not have been possible. We extend special thanks to our heroic winter-overs during the observing seasons up until 2018: Robert Schwarz, Steffen Richter, Sam Harrison, Grantland Hall, and Hans Boenish. We thank all those who have contributed past efforts to the BICEP/Keck series of experiments, including the BICEP1 team. We also thank the *Planck* and WMAP teams for the use of their data.

We are grateful to Johannes Eskilt, Kai Murai, Laura Herold, and Alessandro Greco for insightful discussions.

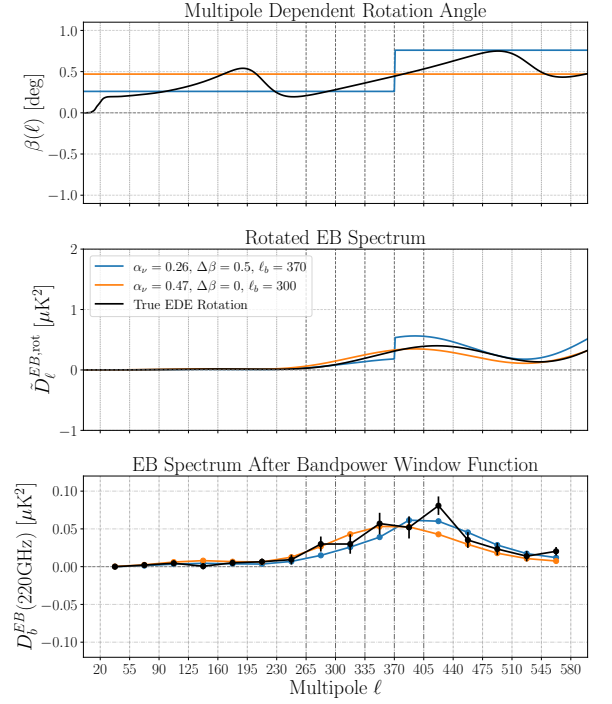
-
- [1] F. Finelli and M. Galaverni, Rotation of Linear Polarization Plane and Circular Polarization from Cosmological Pseudoscalar Fields, *Phys. Rev. D* **79**, 063002 (2009).
 - [2] Y. Minami and E. Komatsu, New Extraction of the Cosmic Birefringence from the Planck 2018 Polarization Data, *Phys. Rev. Lett.* **125**, 221301 (2020).
 - [3] J. Q. Xia, H. Li, and X. Zhang, Probing CPT violation with CMB polarization measurements, *Phys. Lett. B* **687**, 129 (2010).
 - [4] P. Diego-Palazuelos, J. R. Eskilt, Y. Minami, *et al.*, Cosmic Birefringence from Planck Data Release 4, *Phys. Rev. Lett.* **130**, 141001 (2022).
 - [5] J. R. Eskilt and E. Komatsu, Improved Constraints on Cosmic Birefringence from the WMAP and Planck Cosmic Microwave Background Polarization Data, *Phys. Rev. D* **106**, 063503 (2022).
 - [6] G.-C. Liu, S. Lee, and K.-W. Ng, Effect on Cosmic Microwave Background Polarization of Coupling of Quintessence to Pseudoscalar Fields, *Phys. Rev. Lett.* **97**, 161303 (2006).
 - [7] S. M. Carroll, G. B. Field, and R. Jackiw, Limits on a Lorentz- and Parity-Violating Modification of Electrodynamics, *Phys. Rev. D* **41**, 1231 (1990).
 - [8] A. Greco, N. Bartolo, and A. Gruppuso, A New Solution for the Observed Isotropic Cosmic Birefringence Angle and its Implications for the Anisotropic Counterpart through a Boltzmann Approach, *J. Cosmol. Astropart. Phys.* **10**, 028.
 - [9] T. Fujita, K. Murai, H. Nakatsuka, and S. Tsujikawa, Detection of isotropic cosmic birefringence and its implications for axionlike particles including dark energy, *Phys. Rev. D* **103**, 043509 (2021).
 - [10] S. Nakagawa, F. Takahashi, and W. Yin, Early dark energy by dark Higgs, and axion-induced non-thermal trapping, *Phys. Rev. D* **107**, 063016 (2023).
 - [11] D. Harari and P. Sikivie, Effects of a Nambu-Goldstone boson on the polarization of radio galaxies and the cosmic microwave background, *Phys. Lett. B* **289**, 67 (1992).
 - [12] M. Kamionkowski, A. Kosowsky, and A. Stebbins, A Probe of Primordial Gravity Waves and Vorticity, *Phys. Rev. Lett.* **78**, 2058 (1997).
 - [13] M. Zaldarriaga and U. Seljak, All-sky analysis of polarization in the microwave background, *Phys. Rev. D* **55**, 1830 (1997).
 - [14] BICEP/Keck and Planck Collaborations, P. A. R. Ade, N. Aghanim, *et al.*, A Joint Analysis of BICEP2/Keck Array and Planck Data, *Phys. Rev. Lett.* **114**, 101301 (2015).
 - [15] A. Lue, L. Wang, and M. Kamionkowski, Cosmological Signature of New Parity-Violating Interactions, *Phys. Rev. Lett.* **83**, 1506 (1999).
 - [16] M. Kamionkowski, How to De-Rotate the Cosmic Microwave Background Polarization, *Phys. Rev. Lett.* **102**, 111302 (2009).
 - [17] E. Y. S. Wu, P. Ade, J. Bock, *et al.*, Parity Violation Constraints Using Cosmic Microwave Background Polarization Spectra from QUAID, *Phys. Rev. Lett.* **102**, 161302 (2009).
 - [18] BICEP/Keck Collaboration, P. A. R. Ade, Z. Ahmed, *et al.*, BICEP/Keck XVIII: Measurement of BICEP3 polarization angles and consequences for constraining cosmic birefringence and inflation, *Phys. Rev. D* **111**, 063505 (2025).
 - [19] J. Cornelison, C. Vergès, P. A. R. Ade, Z. Ahmed, M. Amiri, *et al.*, Improved polarization calibration of the BICEP3 CMB polarimeter at the south pole, in *SPIE Astronomical Telescopes + Instrumentation 2022* (2022) p. 121901X.
 - [20] F. Bianchini, W. L. K. Wu, *et al.*, Searching for Anisotropic Cosmic Birefringence with Polarization Data from SPTpol, *Phys. Rev. D* **102**, 083504 (2020).
 - [21] D. Contreras, P. Boubel, and D. Scott, Constraints on direction-dependent cosmic birefringence from planck polarization data, *Journal of Cosmology and Astroparticle Physics* **2017** (12), 046.
 - [22] K. R. Ferguson, A. J. Anderson, N. Whitehorn, *et al.*,

- Searching for axion-like time-dependent cosmic birefringence with data from SPT-3G, *Phys. Rev. D* **106**, 042011 (2022).
- [23] BICEP2 / Keck Array Collaboration, P. A. R. Ade, Z. Ahmed, *et al.*, BICEP2 / Keck Array IX: New bounds on anisotropies of CMB polarization rotation and implications for axionlike particles and primordial magnetic fields, *Phys. Rev. D* **96**, 102003 (2017).
- [24] BICEP / Keck Collaboration, P. A. R. Ade, Z. Ahmed, *et al.*, BICEP / Keck XII: Constraints on axion-like polarization oscillations in the cosmic microwave background, *Phys. Rev. D* **103**, 042002 (2021).
- [25] BICEP / Keck Collaboration, P. A. R. Ade, Z. Ahmed, *et al.*, BICEP / Keck XIV: Improved constraints on axion-like polarization oscillations in the cosmic microwave background, *Phys. Rev. D* **105**, 022006 (2022).
- [26] BICEP / Keck Collaboration, P. A. R. Ade, Z. Ahmed, *et al.*, BICEP / Keck XVII: Line of Sight Distortion Analysis: Estimates of Gravitational Lensing, Anisotropic Cosmic Birefringence, Patchy Reionization, and Systematic Errors, *Astrophys. J.* **949**, 43 (2023).
- [27] A. J. Cukierman, S. E. Clark, and G. Halal, Magnetic Misalignment of Interstellar Dust Filaments, *Astrophys. J.* **946**, 106 (2023).
- [28] J. R. Eskilt, L. Herold, E. Komatsu, *et al.*, Constraint on Early Dark Energy from Isotropic Cosmic Birefringence, *Astron. Astrophys.* **675**, A89 (2023).
- [29] K. Murai, F. Naokawa, T. Namikawa, and E. Komatsu, Isotropic cosmic birefringence from early dark energy, *Phys. Rev. D* **107**, L041302 (2023).
- [30] J. L. Bernal, L. Verde, and A. G. Riess, The trouble with H_0 , *J. Cosmol. Astropart. Phys.* **10**, 019.
- [31] B. D. Sherwin and T. Namikawa, Cosmic birefringence tomography and calibration-independence with reionization signals in the CMB, *Mon. Not. Roy. Astron. Soc.* **520**, 3298 (2023).
- [32] T. Karwal and M. Kamionkowski, Dark energy at early times, the Hubble tension, and the string axiverse, *Phys. Rev. D* **94**, 103523 (2016).
- [33] L. Herold, E. G. M. Ferreira, and E. Komatsu, New constraint on Early Dark Energy from Planck and BOSS data using the profile likelihood, *Astrophys. J. Lett.* **929**, L16 (2022).
- [34] T. L. Smith, V. Poulin, J. L. Bernal, *et al.*, Early dark energy is not excluded by current large-scale structure data, *Phys. Rev. D* **103**, 123542 (2021).
- [35] A. Reeves, L. Herold, S. Vagnozzi, *et al.*, Restoring cosmological concordance with early dark energy and massive neutrinos?, *Mon. Not. Roy. Astron. Soc.* **520**, 3688 (2023).
- [36] L. Herold, *Resolving the Hubble tension with Early Dark Energy*, Ph.D. thesis, Ludwig-Maximilians-Universität München, Munich, Germany (2023).
- [37] V. Poulin, T. L. Smith, and T. Karwal, The Ups and Downs of Early Dark Energy solutions to the Hubble tension: a review of models, hints and constraints circa 2023, *Phys. Rep.* **1032**, 1 (2023).
- [38] H. Nakatsuka, T. Namikawa, and E. Komatsu, Is cosmic birefringence due to dark energy or dark matter? A tomographic approach, *Phys. Rev. D* **105**, 123509 (2022).
- [39] J. C. Hill, E. Calabrese, S. Aiola, *et al.*, The Atacama Cosmology Telescope: Constraints on Pre-Recombination Early Dark Energy, *Phys. Rev. D* **105**, 123536 (2022).
- [40] BICEP/Keck Collaboration, P. A. R. Ade, Z. Ahmed, *et al.*, BICEP/Keck XIII: Improved Constraints on Primordial Gravitational Waves using Planck, WMAP, and BICEP/Keck Observations through the 2018 Observing Season, *Phys. Rev. Lett.* **127**, 151301 (2021).
- [41] Planck Collaboration, P. A. R. Ade, N. Aghanim, *et al.*, Planck 2015 results. XIX. Constraints on primordial magnetic fields, *Astron. Astrophys.* **594**, A19 (2016).
- [42] A. Lewis, A. Challinor, and A. Lasenby, Efficient Computation of CMB anisotropies in closed FRW models, *Astrophys. J.* **538**, 473 (2000).
- [43] Planck Collaboration, P. Ade, N. Aghanim, *et al.*, Planck 2013 results. XVI. Cosmological parameters, *Astron. Astrophys.* **571**, A16 (2014).
- [44] D. Blas, J. Lesgourgues, and T. Tram, The Cosmic Linear Anisotropy Solving System (CLASS) II: Approximation schemes, *J. Cosmol. Astropart. Phys.* **07**, 034.
- [45] B. Feng, H. Li, M. Li, and X. Zhang, Gravitational Leptogenesis and Its Signatures in CMB, *Phys. Lett. B* **620**, 27 (2005).
- [46] H. Cai and Y. Guan, Computing microwave background polarization power spectra from cosmic birefringence, *Phys. Rev. D* **105**, 063536 (2022).
- [47] BICEP/Keck Collaboration, P. A. R. Ade, Z. Ahmed, *et al.*, BICEP2 / Keck Array X: Constraints on Primordial Gravitational Waves Using Planck, WMAP, and New BICEP2/Keck Observations through the 2015 Season, *Phys. Rev. Lett.* **121**, 221301 (2018).
- [48] V. Poulin, T. L. Smith, T. Karwal, and M. Kamionkowski, Early Dark Energy Can Resolve The Hubble Tension, *Phys. Rev. Lett.* **122**, 221301 (2019).
- [49] E. Calabrese, J. C. Hill, H. T. Jensen, *et al.*, The Atacama Cosmology Telescope: DR6 Constraints on Extended Cosmological Models, *J. Cosmol. Astropart. Phys.* **10**, 082.
- [50] J. Torrado and A. Lewis, Cobaya: Code for Bayesian Analysis of hierarchical physical models, *J. Cosmol. Astropart. Phys.* **05**, 057.
- [51] A. Gelman and D. B. Rubin, Inference from Iterative Simulation Using Multiple Sequences, *Statist. Sci.* **7**, 457 (1992).
- [52] J. Dunkley, M. Bucher, P. G. Ferreira, K. Moodley, and C. Skordis, Fast and reliable Markov chain Monte Carlo technique for cosmological parameter estimation, *Mon. Not. Roy. Astron. Soc.* **356**, 925 (2005), [astro-ph/0405462](https://arxiv.org/abs/astro-ph/0405462).
- [53] Planck Collaboration, Planck 2018 Results. III. High Frequency Instrument Data Processing and Frequency Maps, *Astron. Astrophys.* **641**, A3 (2020).
- [54] BICEP/Keck Collaboration, P. A. R. Ade, Z. Ahmed, *et al.*, BICEP2 / Keck Array VII: Matrix Based E/B Separation Applied to BICEP2 and the Keck Array, *Astrophys. J.* **825**, 66 (2016).
- [55] BICEP2 Collaboration, P. A. R. Ade, R. W. Aikin, *et al.*, BICEP2 I: Detection of B-mode Polarization at Degree Angular Scales, *Phys. Rev. Lett.* **112**, 241101 (2014).
- [56] G. E. Addison, C. L. Bennett, M. Halpern, G. Hinshaw, and J. L. Weiland, Revisiting the A_L Lensing Anomaly in Planck 2018 Temperature Data, *Astrophys. J.* **961**, 161 (2024).

Appendix: Supplementary Figures and Table

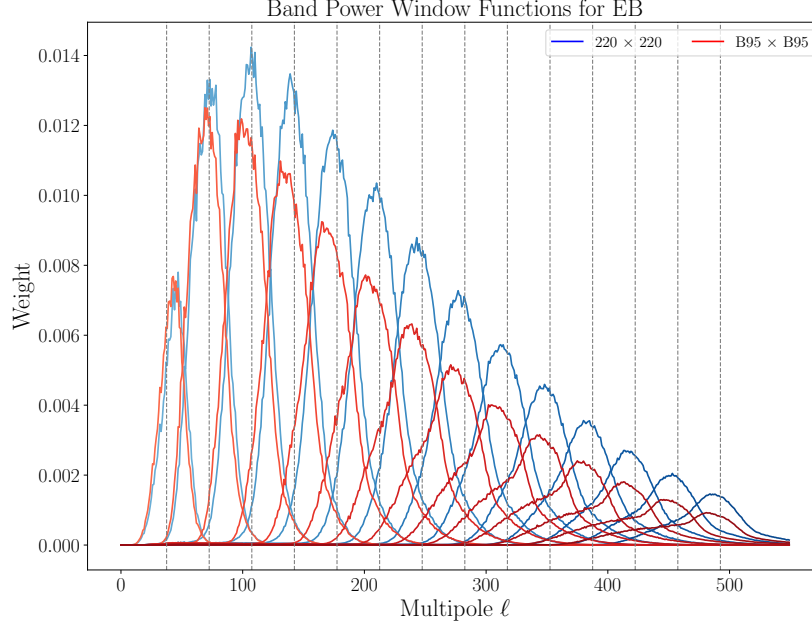


(a) Examples of $\beta(\ell)$ modeled as step functions at various breakpoints ℓ_b . Each curve represents a different step size $\Delta\beta_{\ell_b}$, demonstrating the effect of multipole-dependent changes in the polarization rotation angle.



(b) Comparison between a step-function $\beta(\ell)$ model (orange) and a constant-angle model (blue), fit to simulated EDE EB data, sim 79 (black). The step function yields a preferred fit to the ℓ -dependent features compared to the constant rotation model ($\chi^2 = 17.1$ vs 18.3).

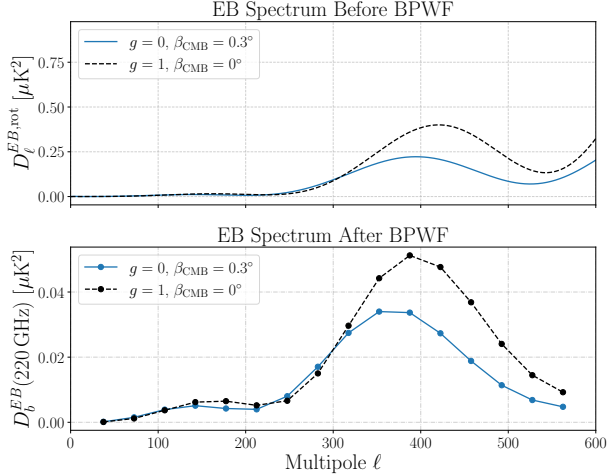
FIG. S1: **Visualizing step-function modeling of ℓ -dependent rotation.** (a) Example $\beta(\ell)$ profile and resulting EB bandpowers after processing through the pipeline. (b) Compared to a constant rotation angle, step function $\beta(\ell)$ demonstrates improved fit to simulated EB spectra from an EDE scenario. In both cases, g is set to zero so the EB spectrum is solely produced by this effective rotation.



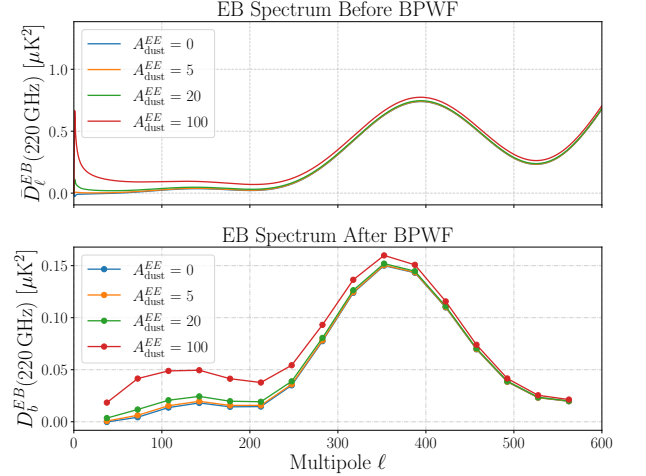
Bandpower #	Nominal ℓ Center
1	37.5
2	72.5
3	107.5
4	142.5
5	177.5
6	212.5
7	247.5
8	282.5
9	317.5
10	352.5
11	387.5
12	422.5
13	457.5
14	492.5

(a) Bandpower window functions (BPWFs) for selected cross spectra, showing contribution to each bandpower across ℓ . Dashed lines correspond to nominal bandpower centers.

(b) Nominal band centers ℓ associated with each bandpower. The theoretical expectation values are calculated via the full convolution with the window functions shown in Figure S2a according to Eq. (15).



(c) Effect of BPWF on EB spectra for varying g and β_{CMB} . No dust or per-band rotation applied.

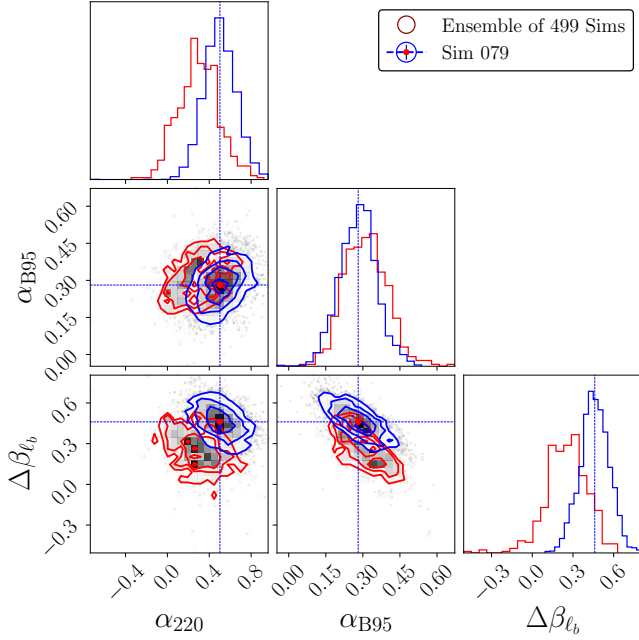


(d) Effect of BPWF on EB spectra with varying dust foreground parameters.

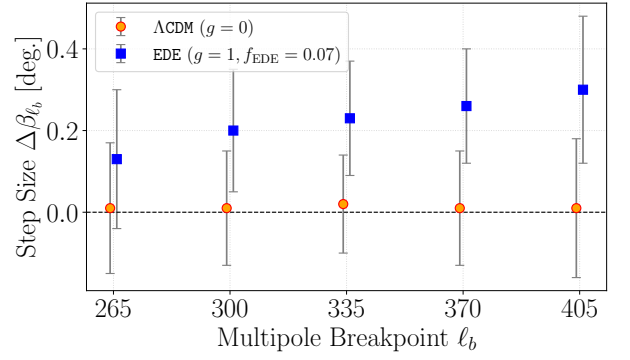
FIG. S2: **Visualizations of the Band Power Window Function and its effect on polarization spectra.** (a) Examples of BPWF shapes and (b) the corresponding bandpower center multipoles used for theoretical spectrum binning. (c-d) Impact of bandpower window function convolution on EB spectra under different parameter variations. Unspecified parameters are set to fiducial values (Table S2). Due to suppression factors from instrumental and analysis filtering, the binned spectra in the lower panels appear at a reduced amplitude relative to the theory spectra.

TABLE S1: **Validation of step-function estimator.** The mean and 68% credible interval of all recovered $\Delta\beta_{\ell_b}$ values (degrees) for each tested breakpoint ℓ_b over the 499 simulation realizations. These recovered values validate that the estimator can accurately constrain multipole dependence when none is present (null Λ CDM case) and detect multipole dependence when it is present in data (EDE case). The distribution of recovered $\Delta\beta_{\ell_b}$ means for $\ell_b = 370$ is shown in contour plot Figure S3a.

Stepfunction Breakpoint (ℓ_b)	baseline ($g = 0$)	EDE ($g = 1$)
265	0.01 ± 0.16	0.13 ± 0.17
300	0.01 ± 0.14	0.20 ± 0.15
335	0.02 ± 0.12	0.23 ± 0.14
370	0.01 ± 0.14	0.26 ± 0.14
405	0.01 ± 0.17	0.30 ± 0.18



(a) Sim 79 overlaid on ensemble of recovered means.



(b) Recovered ensemble $\Delta\beta_{\ell_b}$ across all multipole breakpoints ℓ_b .

FIG. S3: **Validation of the model-independent step-function estimator.** (a) Posterior distribution (where shaded regions represent 2D MCMC sample densities, and the contours represent the 68%, 95%, and 99% credible intervals) of the step amplitude $\Delta\beta_{\ell_b}$ for a single EDE realization overlaid on the ensemble distribution of posterior means from 499 simulations (red). The blue dashed lines indicate the specific posterior mean for the representative realization (Sim 79), marking its position on the ensemble distribution with a red dot. (b) Recovered step amplitudes $\Delta\beta_{\ell_b}$ across all tested multipole breakpoints. Points represent the average of the 499 posterior means, while error bars represent the 68% credible interval. The **baseline** set (blue) consistently recovers zero, while the **EDE** set (red) exhibits a nonzero, ℓ -dependent signal characteristic of the injected birefringence.

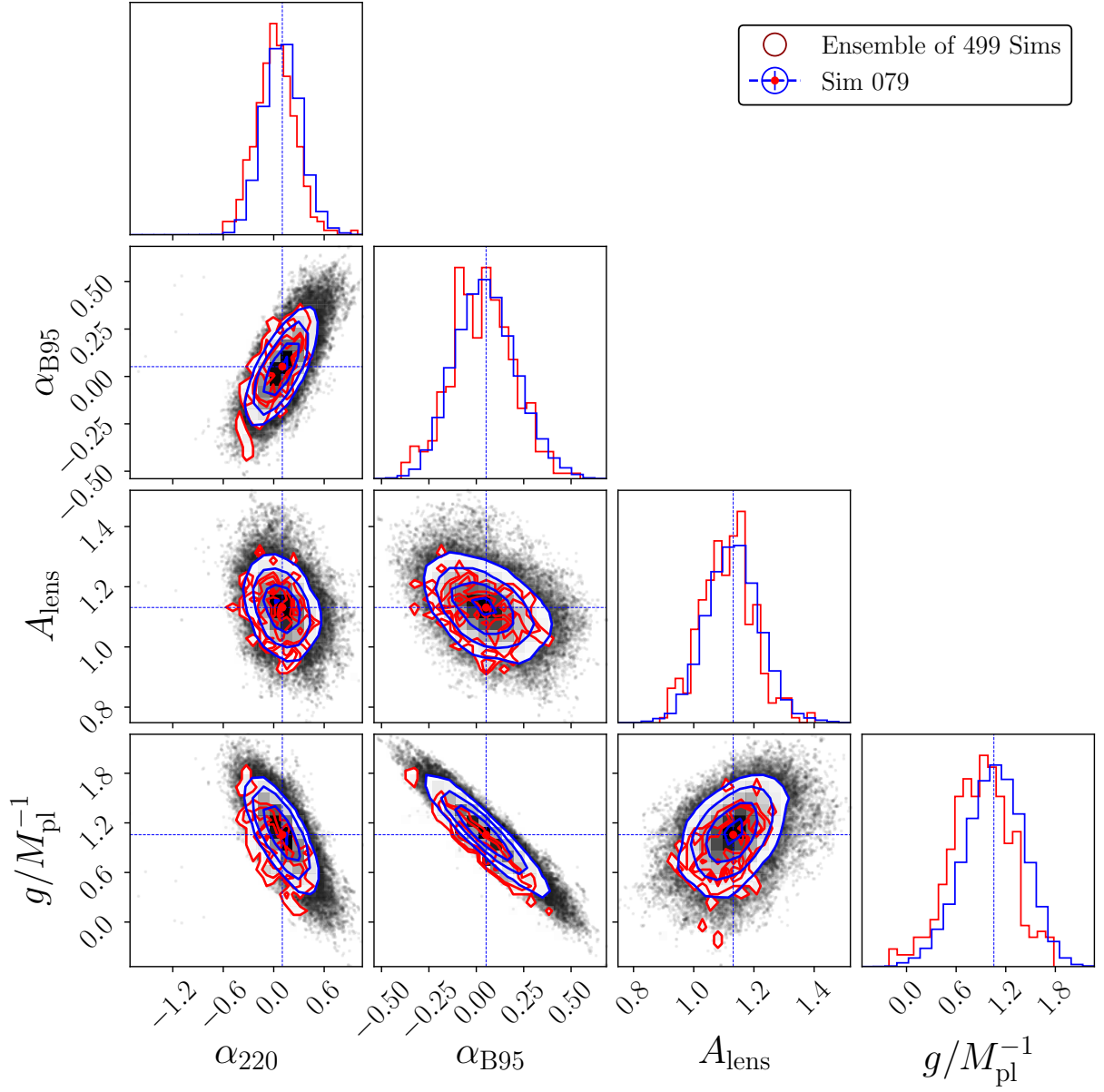


FIG. S4: **Validation of parameter constraints for the EDE estimator.** Contours show the posterior from a single representative realization (blue) compared to the distribution of best-fit peaks from 499 simulations (red) in the EDE set (“All with scaled BB”). The agreement between the single-realization width and the ensemble scatter indicates that the likelihood accurately estimates parameter uncertainties. Blue dashed lines mark the mean of Sim 79 realization’s posterior, and the red dot marks its position on the ensemble contour. For visualization, the posterior is projected onto select parameters of interest; all other foreground and instrument parameters (see Tables S2 and S3) are marginalized over.

TABLE S2: **Validation of parameter recovery on null (baseline) simulations.** Values represent the mean and 68% credible interval of the ensemble of 499 individual posterior means recovered from the **baseline** simulation sets. All recovered means are consistent with the fiducial input. The rotation angles are in units of degrees, g is in units of M_{pl}^{-1} , and dust amplitudes are in units of μK^2 . The spectral indices are unitless.

Parameter	All with free A_{lens}	All	No BB	EB only	Fiducial
g	0.03 ± 0.31	0.03 ± 0.35	0.05 ± 0.40	0.03 ± 0.40	0
α_{220}	-0.01 ± 0.22	-0.00 ± 0.21	-0.01 ± 0.23	-0.01 ± 0.23	0
α_{150}	-0.02 ± 0.17	-0.01 ± 0.17	-0.02 ± 0.18	-0.02 ± 0.18	0
α_{K95}	0.02 ± 0.27	0.00 ± 0.24	-0.01 ± 0.25	-0.00 ± 0.25	0
α_{B95lf}	-0.02 ± 0.15	-0.02 ± 0.16	0.03 ± 0.18	-0.00 ± 0.52	0
A_{lens}	1.05 ± 0.08	—	—	—	1
A_{dust}^{EE}	7.7 ± 1.3	7.49 ± 1.58	8.05 ± 2.07	—	7.5
$\alpha_{\text{dust}}^{EE}$	-0.33 ± 0.18	-0.28 ± 0.26	-0.30 ± 0.25	—	-0.4
A_{dust}^{BB}	3.86 ± 0.8	4.22 ± 1.12	—	—	3.75
$\alpha_{\text{dust}}^{BB}$	-0.31 ± 0.18	-0.24 ± 0.26	—	—	-0.4
A_{dust}^{EB}	0.00 ± 0.40	0.00 ± 0.41	-0.01 ± 0.46	-0.01 ± 0.49	0
β_{dust}	1.68 ± 0.15	1.68 ± 0.16	1.72 ± 0.28	—	1.6

TABLE S3: **Validation of parameter recovery on birefringent (EDE) simulations.** Values represent the mean and 68% credible interval of the ensemble of 499 individual posterior means recovered from the EDE simulation sets. The estimator recovers the injected signal across most configurations without bias. Selected parameters are shown in Fig. S4. The rotation angles are in units of degrees, g is in units of M_{pl}^{-1} , and dust amplitudes are in units of μK^2 . The spectral indices are unitless.

Parameter	All with free A_{lens}	All	No BB	EB only	Fiducial
g	0.89 ± 0.36	0.71 ± 0.32	0.98 ± 0.40	1.00 ± 0.40	1
α_{220}	0.02 ± 0.22	0.10 ± 0.20	-0.02 ± 0.23	-0.02 ± 0.24	0
α_{150}	0.03 ± 0.17	0.12 ± 0.15	0.00 ± 0.18	-0.00 ± 0.19	0
α_{K95}	0.03 ± 0.24	0.11 ± 0.23	-0.01 ± 0.25	-0.01 ± 0.26	0
α_{B95lf}	0.03 ± 0.16	0.12 ± 0.14	-0.02 ± 0.18	0.00 ± 0.18	0
A_{lens}	1.11 ± 0.09	—	—	—	1
A_{dust}^{EE}	7.88 ± 1.45	7.32 ± 1.46	7.93 ± 1.98	—	7.5
$\alpha_{\text{dust}}^{EE}$	-0.38 ± 0.21	-0.31 ± 0.25	-0.34 ± 0.24	—	-0.4
A_{dust}^{BB}	3.84 ± 0.84	3.60 ± 0.84	—	—	3.75
$\alpha_{\text{dust}}^{BB}$	-0.37 ± 0.24	-0.28 ± 0.25	—	—	-0.4
A_{dust}^{EB}	0.03 ± 0.51	0.01 ± 0.38	0.02 ± 0.44	0.02 ± 0.48	0
β_{dust}	1.66 ± 0.16	1.61 ± 0.16	1.68 ± 0.28	—	1.6

TABLE S4: **Sensitivity of parameter recovery to the assumed EDE template shape.** Comparison of recovered angles α_ν and coupling g when using different initial theory templates (f_{EDE}) for analysis across the 499 simulation realizations. In the null case (**baseline**, left), recovery is robust against template choice. In the signal case ($g = 1$, right), slight biases appear if the analysis template differs from the true underlying signal, demonstrating the need for a model-independent estimator.

Parameter	baseline $g = 0$				EDE $g = 1$			
	Template f_{EDE}				Template f_{EDE}			
	0.012	0.070	0.087	0.127	0.012	0.070	0.087	0.127
α_{220}	-0.00 ± 0.21	-0.02 ± 0.27	-0.01 ± 0.22	0 ± 0.17	0.20 ± 0.21	0 ± 0.30	0.13 ± 0.23	0.34 ± 0.19
α_{150}	-0.01 ± 0.14	-0.02 ± 0.21	-0.01 ± 0.16	0 ± 0.10	0.20 ± 0.15	0 ± 0.23	0.12 ± 0.16	0.35 ± 0.10
α_{K95}	-0.02 ± 0.25	-0.03 ± 0.32	-0.04 ± 0.26	-0.01 ± 0.23	0.19 ± 0.24	0 ± 0.29	0.12 ± 0.25	0.35 ± 0.23
α_{B95lf}	-0.01 ± 0.13	-0.03 ± 0.22	-0.01 ± 0.15	-0.01 ± 0.07	0.20 ± 0.13	0 ± 0.23	0.13 ± 0.15	0.36 ± 0.07
g	0.11 ± 1.1	0.02 ± 0.46	0.04 ± 0.41	0.03 ± 0.35	2.29 ± 1.2	0.97 ± 0.45	0.89 ± 0.42	0.75 ± 0.37

TABLE S5: **Systematics and robustness checks for dust.** Recovered g values across 499 simulation realizations when analyzing null simulations generated with different non-Gaussian dust models; no significant bias is observed. Same labels as in Ref. [40] are used for the alternate dust models.

Dust Simulation Dataset	Recovered g
No Dust	0.04 ± 0.31
Gaussian Dust	0.03 ± 0.31
pysm1	-0.02 ± 0.35
pysm2	0 ± 0.46
pysm3	-0.03 ± 0.38
mhd	-0.07 ± 0.33
mkd	0.13 ± 0.35
gdecorr	0.04 ± 0.32
gampmod	0.03 ± 0.32
vansyngel	0.05 ± 0.31

TABLE S6: **Robustness against injected detector rotation.** (a) For each configuration, the specific rotation angles (in degrees) injected into each frequency of all simulation realizations. (b) The mean and 68% credible interval of the recovered coupling constant g (in M_{pl}^{-1}) for each configuration across 499 realizations. The consistency of the recovered values demonstrates that the estimator separates instrumental rotation from the EDE signal without bias.

(a) Injected detector rotation					(b) Recovered coupling g		
Configuration	220	150	K95	B95lf	Configuration	baseline	EDE
Positive	0	0.25	0.5	0.75	Positive	0.04 ± 0.37	0.97 ± 0.42
Negative	0	-0.25	-0.5	-0.75	Negative	0.03 ± 0.38	0.98 ± 0.42
Balanced	-1	-0.5	0	0.5	Balanced	0.03 ± 0.37	0.97 ± 0.42
Null injection	0	0	0	0	Null injection	0.03 ± 0.37	0.97 ± 0.41